Forcing of recent decadal variability in the Equatorial and North Indian Ocean

P. R. Thompson[1], C. G. Piecuch[2], M. A. Merrifield[1], J. P. McCreary[3], and E. Firing[1]

[1]Department of Oceanography, University of Hawaii at Mānoa, Honoululu, Hawaii, USA, [2]Atmospheric and Environmental Research, Inc., Lexington, Massachusetts, USA, [3]International Pacific Research Center, University of Hawaii at Mānoa, Honoululu, Hawaii, USA

Abstract Recent decadal sea surface height (SSH) variability across the Equatorial and North Indian Ocean (ENIO, north of 5°S) is spatially coherent and related to a reversal in basin-scale, upper-ocean-temperature trends. Analysis of ocean and forcing fields from a data-assimilating ocean synthesis (ECCOv4) suggests that two equally important mechanisms of wind-driven heat redistribution within the Indian Ocean account for a majority of the decadal variability. The first is the Cross-Equatorial Cell (CEC) forced by zonal wind stress curl at the equator. The wind stress curl variability relates to the strength and position of the Mascarene High, which is influenced by the phase of the Indian Ocean Subtropical Dipole. The second mechanism is deep (700 m) upwelling related to zonal wind stress at the equator that causes deep, cross-equatorial overturning due to the unique geometry of the basin. The CEC acts to cool the upper ocean throughout most of the first decade of satellite altimetry, while the deep upwelling delays and then amplifies the effect of the CEC on SSH. During the subsequent decade, reversals in the forcing anomalies drive warming of the upper ocean and increasing SSH, with the effect of the deep upwelling leading the CEC.

1. Introduction

Shortly after the turn of the century, temperature trends in the equatorial Indian Ocean thermocline reversed sign from negative to positive [*Nieves et al.*, 2015]. In addition, the decadal rate of sea surface height (SSH) change north of 5°S in the Indian Ocean increased by approximately 6 mm/yr from 1993–2003 to 2004–2013 (Figure 1). The timing of the increase coincided with a slowing in the warming rate of global surface temperatures, which has been linked to cooling of Pacific sea surface temperature (SST) over the last 10–15 years [*Kosaka and Xie*, 2013; *England et al.*, 2014; *Nieves et al.*, 2015]. Volume and heat transport in the Indonesian Throughflow (ITF) also increased during this time [*Lee et al.*, 2015], leading to the suggestion that the temperature trend reversal in the equatorial Indian Ocean thermocline represents a redistribution of heat via the ITF from the surface of the Pacific Ocean to subsurface waters of the tropical Indian Ocean [*Nieves et al.*, 2015].

It is not clear how temperature anomalies that enter the eastern Indian Ocean via the ITF at 10–20°S are dynamically connected to upper-ocean temperature variability at equatorial and Northern Hemisphere latitudes of the Indian Ocean. One possible pathway is propagation across the basin as Rossby waves [*Schwarzkopf and Böning*, 2011], where upon reaching the western boundary, the anomalies become entrained into the meridional circulation or propagate equatorward along the coastal waveguide. On the other hand, model experiments suggest that forcing over the Indian Ocean dominates variability in the western half of the basin [*Nidheesh et al.*, 2012; *Trenary and Han*, 2013]. As a result, anomalies originating in the tropical Pacific are likely to be overwhelmed by local forcing over the basin interior, so that the influence of the Pacific anomalies is apparent only in the Southeast Indian Ocean [*Trenary and Han*, 2013].

The purpose of this paper is to increase understanding of the nature and dynamics of recent decadal variability in the Equatorial and North Indian Ocean (ENIO), which we define as the Indian Ocean north of 5°S. We first analyze satellite altimetry data to identify key features of spatial and temporal variability in SSH. We then utilize an ocean state estimate (ECCOv4, described in section 3) to diagnose the temperature budget, dynamics, and forcing of ENIO variability. Analysis of ECCOv4 suggests that meridional and vertical
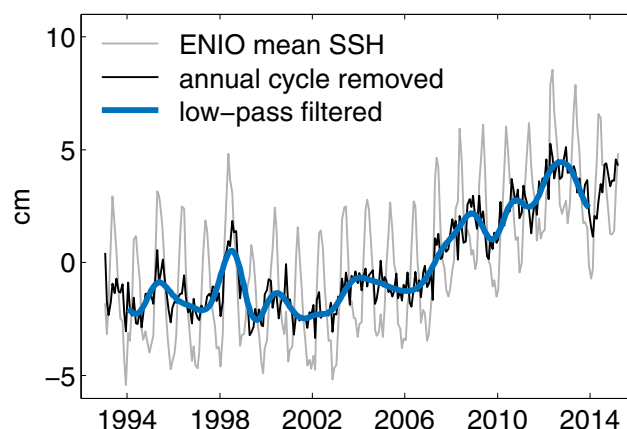
Figure 1. Monthly mean AVISO SSH in the ENIO north of 5°S before filtering (gray), after removal of the mean annual cycle (black), and after applying the low-pass filter (blue).

temperature advection is the most important contribution to recent ENIO decadal variability. Surface fluxes are not negligible, but they do not contribute significantly at decadal time scales. Further, the temperature-advection terms are dynamically linked to features of wind stress variability over the equatorial Indian Ocean. Most importantly, we find that wind-driven velocity anomalies acting on the mean temperature field are the dominant terms in the temperature budget. Thus, recent upper-ocean warming in the ENIO primarily reflects a redistribution of heat within the Indian Ocean and is not likely to be directly linked to temperature anomalies originating in the Pacific.

2. Spatial and Temporal Structure of Observed SSH

In this section, we analyze ENIO SSH variability in AVISO satellite altimetry data during 1993–2015. AVISO distributes a gridded SSH product that combines data from multiple satellite altimetry missions. It is produced by Ssalto/Duacs with support from CNES and is freely available from the AVISO website (http://www.aviso.altimetry.fr/duacs/). We first discuss long-term and decadal trends in the AVISO data set (section 2.1) and then test the coherence of the decadal variability between subregions of the ENIO (section 2.2). We determine that differences between subregions at interannual time scales primarily relate to variations in near-equatorial zonal wind stress. After subtracting variability related to equatorial wind stress, the subregional series show a spatially coherent decadal fluctuation, which motivates the search for other mechanisms that affect mean ENIO SSH variability at decadal time scales.

2.1. Recent SSH Trends

A substantial fraction of the temporal variability in ENIO SSH (Figure 1) and other fields (not shown) occurs at annual and shorter periods. To focus attention on interannual and decadal scales, we first remove the mean annual cycle from the time series by subtracting the climatological mean of each month. We then apply a low-pass filter that passes more than 90% of the amplitude at 24 months and less than 10% of the amplitude at 12 months. To minimize end effects, we ignore the first and last year of each filtered time series. The same filter is utilized throughout this investigation. Applied to the monthly time series of SSH averaged over the ENIO, the filtered time series shows interannual fluctuations with amplitude 1–2 cm superimposed on decadal trends with a net change of about 5 cm over the last two decades (Figure 1).

SSH trends in the ENIO from AVISO are similar to the global-mean rate of approximately 3 mm/yr during the altimetry record (1993–2015, Figure 2a). In contrast, nearby trends in the western tropical Pacific are 2–3 times the global-mean rate due to wind-driven decadal variability [e.g., *Timmermann et al.*, 2010; *Merrifield*, 2011; *Becker et al.*, 2012]. The lack of similarly large SSH trends in the ENIO does not preclude significant wind-driven decadal change in the region, because, as discussed below, decadal variations in the ENIO are not well characterized by a single linear trend over the altimetry record.

Splitting the altimetry record into two decades, 1993–2003 and 2004–2014, demonstrates that decadal rates of ENIO SSH change vary in space and time during the course of the altimetry record (Figures 2b and 2c). Trends during the first decade are weaker, predominantly negative in the west, and predominantly positive in the east. During the second decade, the trends are greater in magnitude and positive in the ENIO region north of about 5°S. The increased rates during the latter decade (5–10 mm/yr) approach recent rates in the western Pacific, but have received much less attention. The time series of SSH anomalies averaged over the ENIO also shows a pronounced inflection in the rate of change that is consistent with the decadal trends discussed above (Figure 3a).
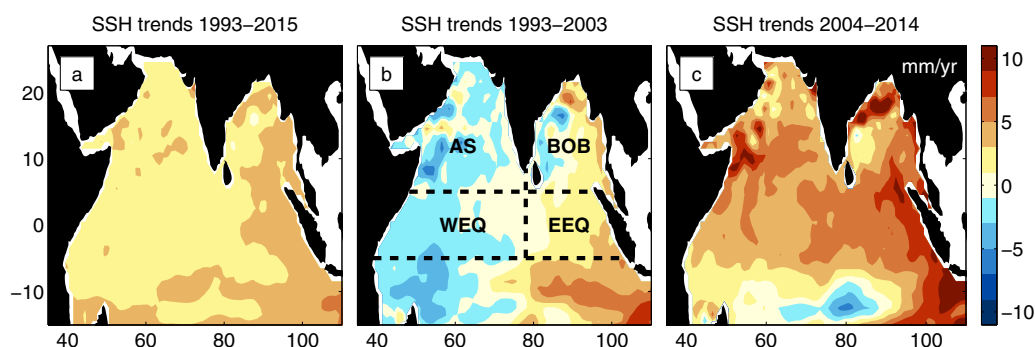
Figure 2. SSH trends from the AVISO multimission gridded product for (a) 1993–2014, (b) 1993–2003, and (c) 2004–2014.

It is tempting to focus on the latter half of the ENIO time series and interpret the increase as enhanced sea level rise (and perhaps ocean warming) in the ENIO during this time. If we subtract global-mean SSH from the ENIO average, however, the variability is best characterized as a decrease relative to the global mean during the first decade followed by a recovery during the second decade (Figure 3b). In general, differences between global-mean and regional-mean SSH can be attributed to wind-driven variability in upper-ocean density, particularly the thermal component [e.g., *Cabanes et al.*, 2001; *Willis et al.*, 2004]. Viewing ENIO SSH relative to the global mean suggests that wind-driven processes may have cooled the ENIO during the earlier period, thereby suppressing the effect of increasing global-ocean volume, while a reversal of this forcing allowed for ENIO SSH to rebound during the latter period.

2.2. Spatial Coherence of the Decadal Variability

In section 3, we treat the ENIO as a control volume and attempt to account for decadal changes in spatial mean SSH and temperature of the region via wind-driven temperature fluxes into the volume. In this section, we motivate this approach by examining the spatial coherence of the decadal SSH variability across the ENIO. We divide the basin into four subregions (demarcated in Figure 2b) and compare mean SSH in each subregion to the mean SSH over the IO north of 5°S (Figure 4a). Substantial differences occur between the subregions at interannual time scales, and while there does appear to be a general depression of SSH during the middle of the record, the interannual variability obscures decadal variation of mean ENIO SSH. Here we attempt to account for the interannual differences between subregions in order to isolate the fraction of decadal variability that is coherent across the ENIO.

An important mode of interannual climate variability in the tropical Indian Ocean is the Indian Ocean Dipole (IOD) [*Saji et al.*, 1999; *Webster et al.*, 1999], which is characterized by an east-west gradient in sea surface temperature (SST) across the basin. The SST gradient results in differential convection that couples to atmospheric circulation in the equatorial region. The atmospheric component of the coupled IOD mode is known as the Equatorial Indian Ocean Oscillation (EQUINOO) [*Gadgil et al.*, 2004], and we capture the structure of
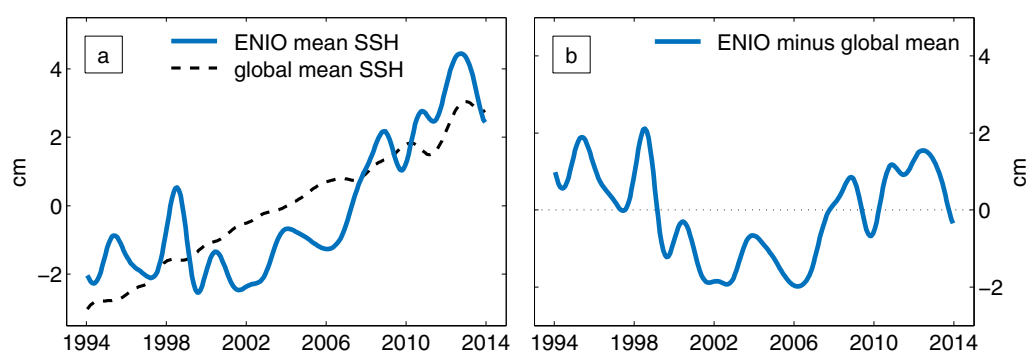

Figure 3. (a) Mean AVISO SSH in the ENIO north of 5°S (blue); global-mean AVISO SSH (black dashed). (b) Mean ENIO SSH minus global-mean SSH.
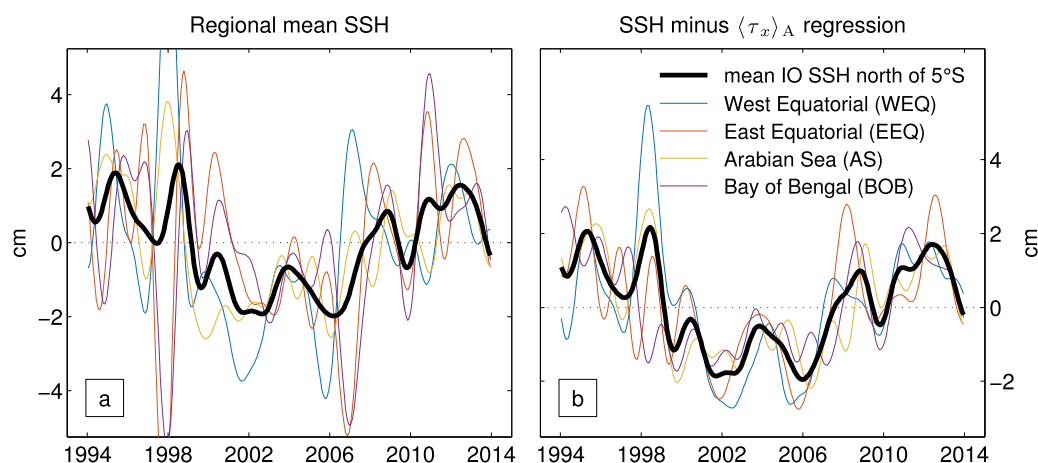
Figure 4. (a) Mean AVISO SSH (global mean removed) over the four regions defined in Figure 2b (colors); mean ENIO SSH north of 5°S (black). (b) Same as Figure 4a after fitting and removing variability accounted for by $\langle \tau_x \rangle_A$ (zonal wind stress averaged over Box A in Figure 5a). Legend in Figure 4b also applies to Figure 4a.

the wind field associated with EQUINOO by regressing low-pass-filtered ERA-Interim wind stress and wind stress curl fields onto zonal wind stress averaged in Box A (3°S–3°N, 46°E–97°E; Figure 5a). In the following, we use the notation $\langle \ \rangle$ to denote spatial averages; e.g., zonal wind stress averaged in Box A is referred to as $\langle \tau_x \rangle_A$.

The response of SSH in the Indian Ocean to the structure in the wind stress field described above is well known in the context of the Madden-Julian Oscillation [*Oliver and Thompson*, 2010; *Webber et al.*, 2010] and at interannual-to-decadal time scales [*Shankar et al.*, 2010; *Nidheesh et al.*, 2012]. Zonal wind stress anomalies at the equator excite Kelvin waves that alter SSH along the equator and, after they reflect from Sumatra, along the eastern boundary. At the same time, the equatorial wind stress and off-equatorial wind stress curl (Figure 5a) excite low-latitude Rossby waves that propagate westward, generating SSH anomalies of the opposite sign in the western half of the basin. Due to the proximity to the equator and relatively narrow basin width, the adjustment time to this forcing (i.e., the time it takes the waves to cross the basin) is less than 2 years [*Shankar et al.*, 2010]. Thus, at periodicities passed by the filter utilized here, we expect that a substantial fraction of the SSH variability of the tropical Indian Ocean is roughly in quasi-equilibrium with the wind forcing. We can then regress AVISO SSH onto $\langle \tau_x \rangle_A$ to obtain the pattern of SSH variability associated with the IOD/EQUINOO variability (Figure 5b).

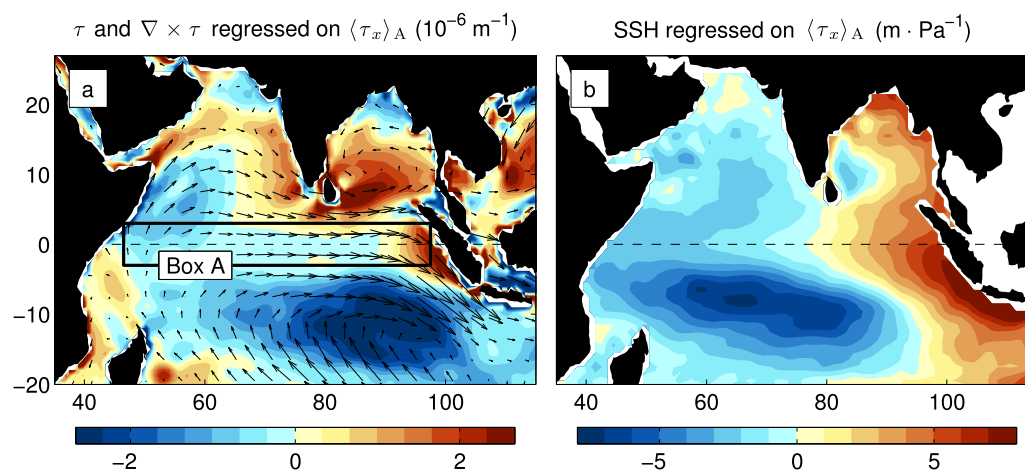**Figure 5.** (a) ERA-Interim vector wind stress and wind stress curl regressed onto equatorial zonal wind stress averaged in Box A ($\langle \tau_x \rangle_A$). The units associated with the color scale (10^{-6} m^{-1}) apply to the curl regression. The regression coefficients of wind stress vectors onto $\langle \tau_x \rangle_A$ are unitless. (b) AVISO SSH anomalies (global mean removed) regressed onto $\langle \tau_x \rangle_A$.

The salient feature of the SSH pattern associated with $\langle \tau_x \rangle_A$ is an east-west gradient across the Indian Ocean, which tends to produce interannual variations with maximum amplitude near the boundaries of the basin and minimum amplitude near the center of the basin [*Shankar et al.*, 2010]. The physical interpretation of this structure is a zonal redistribution of ocean volume in the ENIO due to the baroclinic response of the ocean to equatorial wind stress and off-equatorial wind stress curl. This pattern accounts for the roughly 180° phase difference between eastern (EEQ, BOB) and western (WEQ, AS) SSH variations on interannual time scales (Figure 4a).

To quantify how much of the interannual variability is accounted for by $\langle \tau_x \rangle_A$, we perform a linear, least squares regression of the detrended SSH in each grid cell onto $\langle \tau_x \rangle_A$. We then subtract the best fit of $\langle \tau_x \rangle_A$ to SSH at each location and reform the subregional averages (Figure 4b). The variance reduction is 31% for the western equatorial subregion (WEQ), 43% for the eastern equatorial subregion (EEQ), 40% for the Bay of Bengal (BOB), and 10% for the Arabian Sea (AS). The fit substantially reduces—but does not completely remove—the interannual differences between subregions. We also tried lagging the SSH relative to $\langle \tau_x \rangle_A$ to assess whether relaxing the assumption of quasi-equilibrium reduced the subregional differences. This approach did not prove to be effective, which suggests the remaining interannual variability is likely due to other processes.

In contrast to the subregional time series, the basin-scale mean north of 5°S remains largely unchanged after subtracting variability related to $\langle \tau_x \rangle_A$ (variance reduced by <1%). We conclude that wind forcing related to the IOD primarily leads to intrabasin, interannual variability and does not contribute to spatially coherent, decadal change in the ENIO. The increased coherence of the subregional SSH time series after subtracting variability accounted for by $\langle \tau_x \rangle_A$ motivates a search for forcing mechanisms that drive coherent decadal variations across the subregions of the ENIO.

3. Dynamics of ENIO Decadal Variability

In this section, we diagnose the upper-ocean temperature budget of the ENIO to understand the thermosteric contribution to decadal SSH fluctuations averaged over the region. We begin with a general discussion of our approach (section 3.1), providing overviews of the ECCOv4 ocean state estimate and its temperature budget. We then note that advection dominates the budget in the ENIO (section 3.2) and relate the dominant advective terms to particular aspects of wind stress forcing (section 3.3).

3.1. Methodology
3.1.1. ECCOv4
The Estimating the Circulation and Climate of the Ocean Version 4 (ECCOv4) [*Wunsch and Heimbach*, 2013; *Forget et al.*, 2015] is an optimal solution of the Massachusetts Institute of Technology general circulation model (MITgcm) [*Marshall et al.*, 1997a,1997b], where differences between the model fields and observations are minimized via the adjoint method [*Heimbach et al.*, 2005]. The solution spans 1992–2011, and the model equations include sea ice. The model grid is global (including the Arctic) with 50 vertical layers, 1° zonal resolution, and varying meridional resolution (approximately 1° at midlatitudes and $\frac{1}{3}^{\circ}$ at the equator). A particular advantage of adjoint-based ECCO syntheses is that the solutions obey conservation laws exactly and are free of artificial internal sources or sinks (e.g., of heat, momentum, freshwater, etc.) [*Wunsch and Heimbach*, 2013].

ECCOv4 reproduces the observed interannual and decadal SSH variability in the ENIO quite well (Figure 6). When trends in the ECCOv4 time series are matched to the trend of the Aviso SSH over their common period, the variations in the two time series have similar phase, but the amplitude of the ECCOv4 fluctuations is slightly smaller. The close correspondence justifies using the ocean state estimate to investigate the dynamics of the observed decadal change. Variations in ECCOv4 upper-ocean potential temperature and SSH closely agree in the ENIO (Figure 6), and decomposing ENIO SSH from ECCOv4 into mass, thermosteric, and halosteric contributions shows that the SSH variability in the region is almost entirely due to thermosteric change (not shown).

3.1.2. Temperature Budget
In ECCOv4, the MITgcm is configured to solve the hydrostatic, Boussinesq primitive equations using the z^* rescaled vertical coordinate [*Adcroft and Campin*, 2004; *Campin et al.*, 2008]. Given a vertical coordinate z
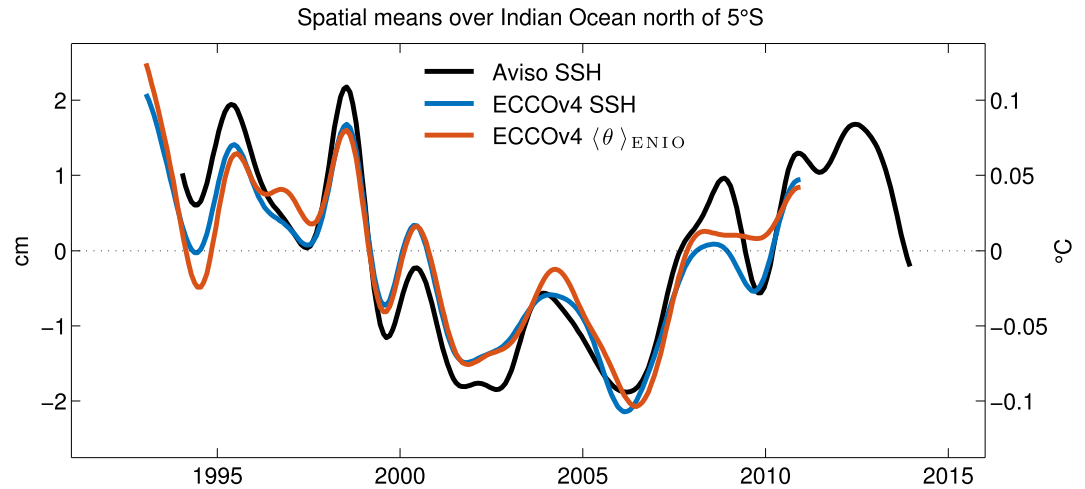
Figure 6. AVISO SSH averaged over the ENIO with global-mean SSH removed (black); ECCOv4 means over the ENIO for SSH with the global mean removed (blue) and ECCOv4 upper-ocean potential temperature ($\langle\theta\rangle_{\mathrm{ENIO}}$, orange). After removing the global-mean time series from the ECCOv4 time series, the trends from ECCOv4 are matched to the trend in AVISO SSH during the period of overlap. The multidecadal trends between the AVISO observations and the ECCOv4 simulation are not identical, but matching the trends over the common period demonstrates the similarity between the two curves at interannual to decadal periods.

with ocean bottom at $z = -H$ and free surface at $z = \eta$, the z^* coordinate is defined as $z^* = (z - \eta)/s^*$, where $s^* = 1 + \eta/H$ is a scaling factor. Note that, by definition, the range of the rescaled vertical coordinate ($z^* \in [-H, 0]$) is time invariant. For a complete description of the model equations in this coordinate system, see *Forget et al.* [2015].

Here we formulate a temperature budget for the ENIO, and we begin with the governing equation for conservation of heat in a model grid cell,

$$\underbrace{\partial_t(s^*\theta)}_{\text{Tendency}} = \underbrace{-[\nabla_{z^*} \cdot (s^*\theta\vec{v}_h) + \partial_{z^*}(\theta w)]}_{\text{Advection}} + \underbrace{s^*\mathcal{F}_\theta}_{\text{Forcing}} + \underbrace{s^*\mathcal{D}_\theta}_{\text{Diffusion}} . \tag{1}$$

In this equation, θ is potential temperature, ∂_t and ∂_{z^*} are the partial derivatives with respect to time and the rescaled vertical coordinate, respectively, ∇_{z^*} is the horizontal gradient operator at constant z^*, $\mathcal{F}_\theta$ is surface forcing, and $\mathcal{D}_\theta$ contains subgrid-scale processes parameterized as diffusive mixing vertically and along isoneutral surfaces. The horizontal and vertical components of velocity ($\vec{v}_h$ and w) include both resolved Eulerian velocity and bolus velocity that parameterizes the effects of unresolved geostrophic eddies [*Gent and Mcwilliams*, 1990]. The surface forcing includes shortwave and longwave radiation, as well as sensible and latent heat flux. All terms in (1) are evaluated on the model grid using appropriate diagnostic output from MITgcm.

We formulate temperature budgets for control volumes spanning the upper 700 m of the ocean. In practice, we use the interface between vertical layers of ECCOv4 that is closest to this depth ($z^* \approx 677$ m). We refer to the upper 700 m potential temperature averaged over the ENIO region north of 5°S as $\langle\theta\rangle_{\mathrm{ENIO}}$. Similarly, we refer to the same quantity averaged over the Indian Ocean north of the equator (NIO) as $\langle\theta\rangle_{\mathrm{NIO}}$.

To express the heat budget for a control volume in terms of a temperature tendency (units of °C s^{-1}), we take the volume integral of (1) and divide by the total volume V,

$$\partial_t\langle\theta\rangle_V \doteq \frac{1}{V}\int_V \partial_t(s^*\theta)dV = \frac{1}{V}\int_V \{-[\nabla_{z^*} \cdot (s^*\theta\vec{v}_h) + \partial_{z^*}(\theta w)] + s^*\mathcal{F}_\theta + s^*\mathcal{D}_\theta\}dV. \tag{2}$$

The above relation serves as a temperature budget that provides time-variable contributions to the rate of change $\partial_t\langle\theta\rangle_V$ from advective, diffusive, and surface fluxes across the horizontal and vertical surfaces of the volume. Note that, since V and s^* vary with time through their dependence on η, $\partial_t\langle\theta\rangle_V$ is not exactly equivalent to the time derivative of the average temperature in the control volume. Because $\theta\partial_t s^*$ is very small compared to $s^*\partial_t\theta$, however, $\partial_t(s^*\theta) \approx s^*\partial_t\theta$ to an extremely good approximation. Therefore, for all practical purposes, the integrated quantity $\partial_t\langle\theta\rangle_V$ can be interpreted as the time tendency of the mean potential temperature in the volume, justifying our notation.
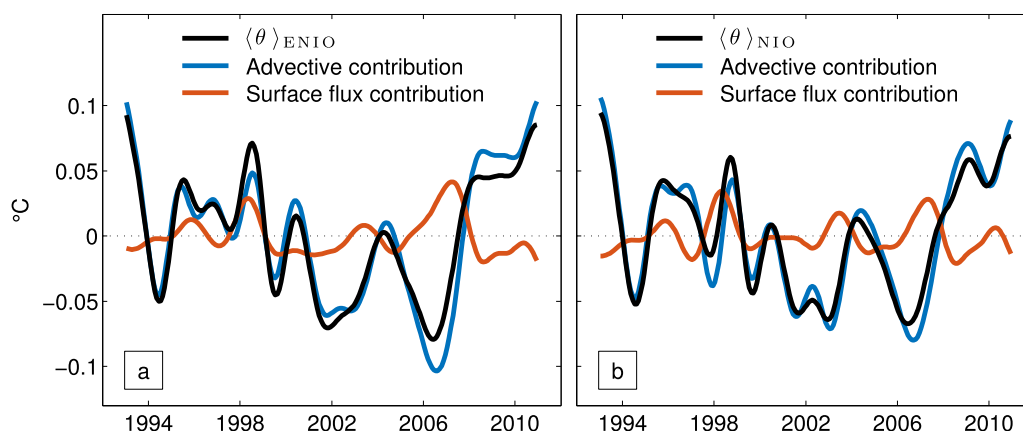
Figure 7. (a) ECCOv4 potential temperature averaged over the upper 700 m of the Indian Ocean north of 5°S (black, $\langle\theta\rangle_{ENIO}$); contribution of advection to $\langle\theta\rangle_{ENIO}$ (blue); contribution of surface fluxes to $\langle\theta\rangle_{ENIO}$ (orange). The mean and linear trend is removed from all three time series. (b) Same as Figure 7a for the Indian Ocean north of the equator (NIO). Diffusive fluxes are negligible in temperature budgets for the ENIO and NIO (not shown).

Following *Lee et al.* [2004], we reference potential temperature in the advective terms to the time-varying mean temperature of the volume, i.e., $\langle\theta\rangle_V$. In the following section, when fluxes are integrated across a fraction of the volume's surface area, volume is not conserved as in (2). Thus, the temporal integrals of individual advective terms are sensitive to the reference temperature. At any given time, temperature flux across some fraction of the volume's surface makes a nonzero contribution to $\partial_t\langle\theta\rangle_V$ only if θ at the interface differs from $\langle\theta\rangle_V$ [*Lee et al.*, 2004]. Thus, referencing temperature to $\langle\theta\rangle_V$ is useful for diagnosing the contribution of fluxes across partial volume interfaces. In practice, the reference temperature for the upper 700 m north of equator is approximately 14.6°C with little variation in time (standard deviation of 0.05°C).

3.1.3. Advective Fluxes

To diagnose the sources of advective flux, we separate the advection term in (2) into contributions across the south, east, west, and bottom faces of the volume. In addition, we decompose advection across each face into anomalous (denoted by primes) and time-mean (overbars, calculated over length of ECCOv4 simulation) components. Using the divergence theorem, we express the advective contributions to the volume integral in (2) as area integrals across each face. For example, advection of potential temperature by meridional velocity (*v*) across the southern face of the volume (i.e., the equator) is the sum of five terms,

$$\frac{1}{V}\int_{A_s}(v\theta)dA_s = \frac{1}{V}\int_{A_s}\left(v'\bar{\theta}+\bar{v}\theta'+(v'\theta')'+\overline{v'\theta'}+\bar{v}\bar{\theta}\right)dA_s, \tag{3}$$

where A_s is the area of the southern face. We decompose advection across the other faces of the volume in a similar fashion. Our focus is on the first three terms on the right-hand side of (3), which are zero-mean contributions to the temporal variability; the fourth and fifth terms are constant. In the following discussion and figures, area integrals and division by volume are implicit in all references to the advective budget terms. We drop the notation associated with these operations for the sake of readability.

3.2. Comparison of Budget Terms

Variability in $\langle\theta\rangle_{ENIO}$ is dominated by the total (horizontal plus vertical) advective flux into the ENIO volume (Figure 7a). The contribution of surface flux is small in comparison, and diffusive flux is negligible (not shown). Restricting the volume to the Indian Ocean north of the equator (NIO), the advective contribution remains dominant (Figure 7b). This result is important, because there are a variety of Indian-Ocean circulations (e.g., East African Coastal Current, South Java Current, Subtropical Overturning Cell) that affect transport across 5°S but do not affect transport across the equator. For this reason, we focus further analysis of the advective contribution on the NIO volume.

Flux of mean temperature across the equator by meridional velocity anomalies, $v'\bar{\theta}$, is the largest advective contribution (Figure 8). The meridional covariance term, $(v'\theta')'$, and the flux of mean temperature into the upper 700 m by vertical velocity anomalies, $w'\bar{\theta}$, make smaller and approximately equal contributions. The
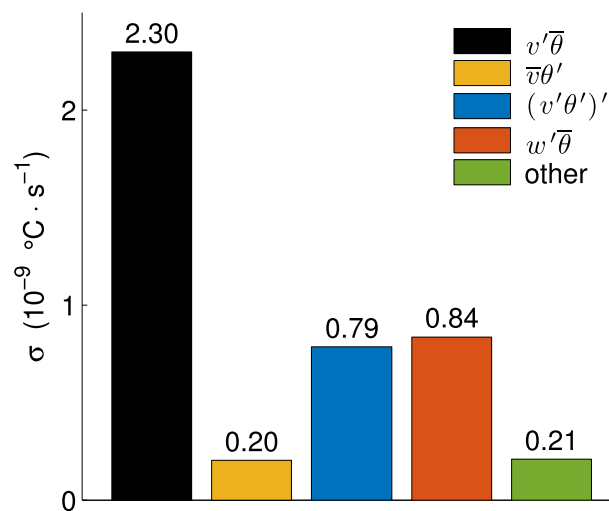
Figure 8. Standard deviation of terms in the decomposition of advective temperature flux.

net contribution from all other advective terms (including small zonal contributions across the east and west faces from the Malacca Strait and Gulf of Aden) is small. These small contributions are difficult to relate to atmospheric forcing, and we do not address them further.

The decadal signal of primary interest is the difference between the SSH trends in two successive decades (Figures 2b and 2c). A step-like difference from one decade to the next in the temperature-tendency terms would correspond to a decadal trend difference in upper-ocean temperature and SSH. Alternatively, one could approximate the decadal variability in Figure 3b using a quadratic polynomial. Indeed, fitting a quadratic to AVISO SSH in each grid cell produces positive quadratic coefficients across the ENIO region, indicating spatially coherent quadratic variability consistent with Figures 2b and 2c. Viewed in this way, positive linear trends in the temperature-tendency terms correspond to quadratic contributions to decadal variation in $\langle\theta\rangle_{NIO}$ and NIO SSH.

It is difficult to visually discern either trends or decadal differences in the temperature-tendency terms due to the presence of substantial interannual variability in these time series (Figure 9a). Unfortunately, the times series are too short to use spectral methods to distinguish between interannual and decadal variability. Instead, we perform a Monte Carlo experiment to determine if the contribution of each tendency term to the reversal in upper-ocean-temperature trends is greater than expected from chance alone. For each tendency term, we calculate the Fourier-transform of the time series and generate an ensemble of realizations by randomizing the phases and then inverse transforming. With 10^4 realizations, a histogram of the trends or the decadal differences provides an empirical probability density function. The location of the actual trend or decadal difference in these distributions gives a rough measure of the degree to which the decadal signal stands out from the interannual background. The 50th percentile in these distributions corresponds to zero trend or decadal difference.

Among the three dominant advective terms, only $v'\overline{\theta}$ has a robust trend and a robust decadal difference, with a positive trend at the 98th percentile of the distribution and a decadal difference at the 94th percentile. Thus, even though the interannual variability visually obscures the lower-frequency changes, there is a robust contribution from the $v'\overline{\theta}$ term to decadal variability in $\langle\theta\rangle_{NIO}$ and NIO SSH. The decadal contribution from $w'\overline{\theta}$ has a weaker positive trend at the 85th percentile and a decadal difference at the 94th percentile. The covariance term, $(v'\theta')'$, adds a weak *negative* trend at the 30th percentile and a decadal difference at the 20th percentile.

The time-integrated sum of these three contributions accounts for 85% of the variance in $\langle\theta\rangle_{NIO}$ (Figure 9b). In this case, we remove the trend and mean from these integrated quantities for direct comparison to the detrended $\langle\theta\rangle_{NIO}$ curve. As expected from the above analysis, the contribution of integrated $v'\overline{\theta}$ dominates the difference in trend from the first to second decade. The other two terms are not well characterized by a quadratic, but they do contain low-frequency variations that are important for reproducing the phasing of the decadal change. For comparison, the variance of the surface flux contribution to upper-ocean temperature is roughly half of the variance in the time-integrated contributions of $(v'\theta')'$ and $w'\overline{\theta}$. The time-integrated contribution of surface flux (Figure 7) shows little decadal-scale variation compared to the advective contributions (Figure 9b).

3.3. Wind Stress Forcing of Advective Budget Terms

In this section, we relate two of the three dominant advective terms to wind stress forcing over the Indian Ocean. We show that the most important advective contribution, $v'\overline{\theta}$, is partially driven by zonal wind stress
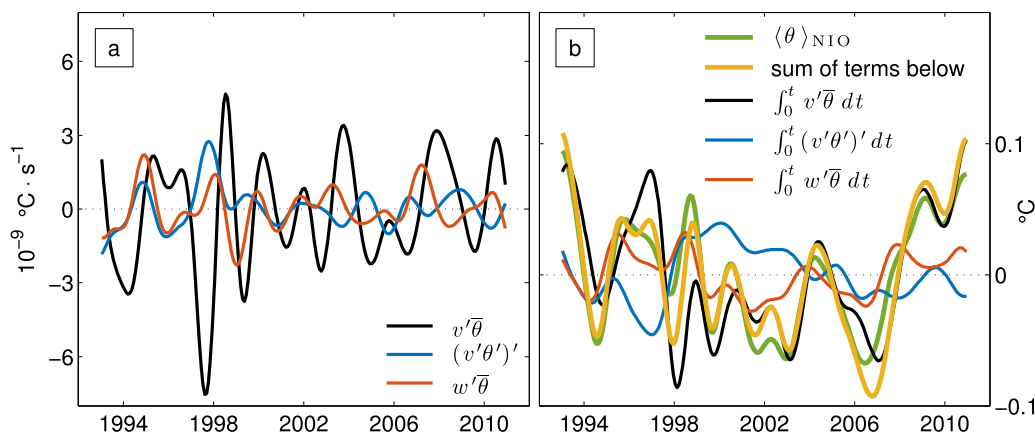
Figure 9. (a) Leading order advective contributions to $\langle\theta\rangle_{\mathrm{NIO}}$: $v'\bar{\theta}$ (black), $(v'\theta')'$ (blue), $w'\bar{\theta}$ (orange). (b) Temporal integrals of the time series on the left (same colors); the sum of the three temporal integrals (yellow); $\langle\theta\rangle_{\mathrm{NIO}}$ (green). The mean and linear trends are removed from the integrated time series in Figure 9b to aid direct comparison to the upper-ocean temperature anomalies.

curl near the equator, which forces variations in the strength of the Indian Ocean Cross-Equatorial Cell (CEC) (section 3.3.1). The contribution of vertical velocity anomalies, $w'\bar{\theta}$, primarily results from the deep signature of Rossby waves forced by the wind pattern correlated with zonal wind stress anomalies on the equator (section 3.3.2). Due to volume conservation, this process also contributes to $v'\bar{\theta}$ via deep cross-equatorial overturning. Finally, we find that the third contribution, $(v'\theta')'$, results from the covariance of annual and higher frequency variability. As a result, this term cannot be readily related to any simple wind-based index (section 3.3.3).

3.3.1. $v'\bar{\theta}$

The primary means of cross-equatorial heat and mass exchange in the Indian Ocean is the CEC [*Miyama et al.*, 2003]. The CEC brings warm surface water southward across the equator in the basin interior, while cold subsurface waters move northward at intermediate depths (200–500 m) along the western boundary. The CEC exports heat from the Northern Hemisphere, and a strengthened CEC corresponds to a reduction of upper-ocean heat content north of the equator. The unique structure of IO equatorial winds, which are primarily antisymmetric about the equator and approximately proportional to latitude, forces the surface branch of the CEC. There is no Ekman pumping associated with this equatorial wind stress curl, and as a result, this forcing generates no geostrophic flow. Thus, the southward interior Sverdrup transport that makes up the surface branch of the CEC is entirely composed of Ekman drift confined to a shallow near-surface layer at the equator [*Miyama et al.*, 2003]. In this case, the Ekman drift is well defined at the equator, because the antisymmetric wind stress vanishes as f goes to zero.

The $v'\bar{\theta}$ term in the temperature budget is highly correlated with cross-equatorial volume transport in the upper 100 m integrated over the width of the basin (hereafter V_{100}, $r = 0.94$, Figure 10a). In order to assess if this surface transport is related to CEC dynamics, we estimate Sverdrup transport across the equator by integrating wind stress curl between 3°S and 3°N over the width of the Indian Ocean,

$$V_{\mathrm{cec}}(t) = \frac{1}{\beta\rho_0} \int_{x_w}^{x_e} \frac{\tau_x(x, 3^\circ\mathrm{S}, t) - \tau_x(x, 3^\circ\mathrm{N}, t)}{L_y}\, dx, \tag{4}$$

where x_w (47°E) and x_e (97°E) are the locations of the western and eastern boundaries, respectively, L_y is the distance between 3°S and 3°N (approximately 660 km), β is the meridional gradient in the Coriolis parameter at the equator (2.3×10^{-11} rad s^{-1} m^{-1}), and ρ_0 is a reference density (1025 kg m^{-3}).

The correlation between V_{100} and V_{cec} calculated from ECCOv4 wind stress is not convincing ($r = 0.52$, not shown together), which we attribute to the complex nature of the circulation near the western boundary that includes recirculations not related to Ekman drift. To test this reasoning, we consider the relationship between V_{cec} and transport in the upper 100 m east of 60°E outside the region affected by recirculations. In this case, the correlation improves drastically ($r = 0.93$, Figure 10b). The correlation is also significant between the transport east of 60°E and V_{cec} calculated from ERA-Interim wind stress, albeit with a reduction in amplitude ($r = 0.78$, Figure 10b).
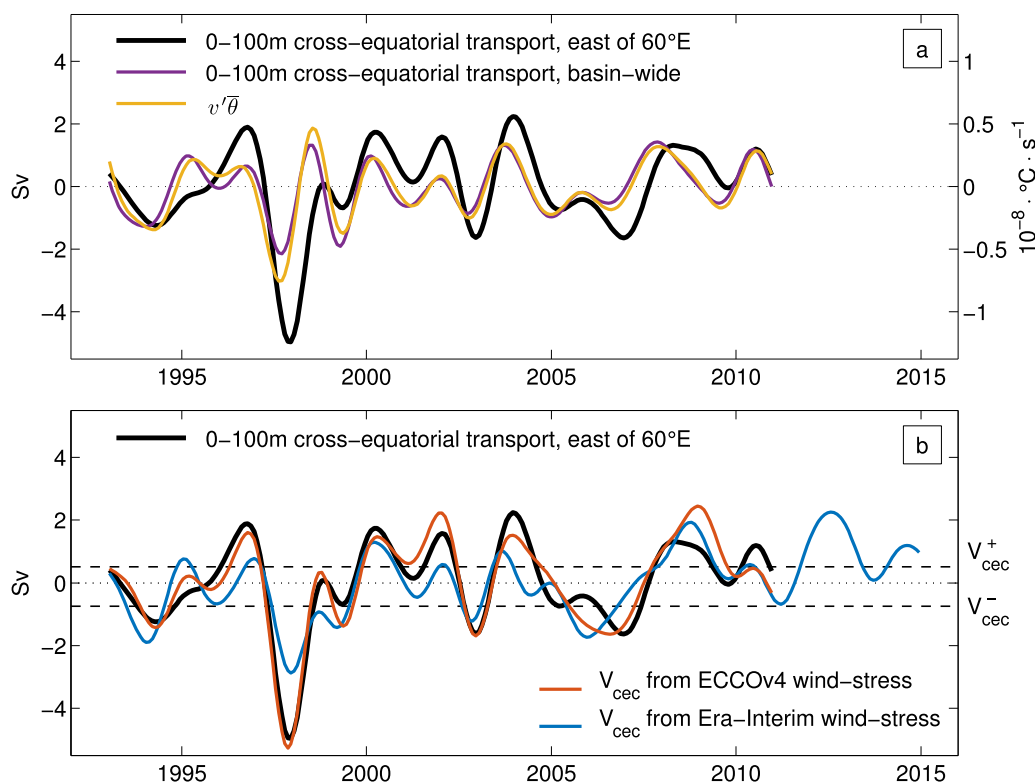
Figure 10. (a) Potential temperature flux across the equator due to advection of mean potential temperature by meridional velocity anomalies ($v'\bar{\theta}$, yellow); anomalies of cross-equatorial 0–100 m volume transport over the width of the basin (purple); anomalies of cross-equatorial 0–100 m volume transport east of 60°E (black). (b) Cross-equatorial Sverdrup transport (V_{cec}) calculated from zonal wind stress fields for ECCOv4 (orange) and ERA-Interim (blue). The upper and lower quartiles of V_{cec} from ERA-Interim are denoted by dashed lines and labeled V_{cec}^+ and V_{cec}^-, respectively.

Despite the agreement between V_{cec} and upper 100 m transport east of 60°E, excluding the western boundary region clearly weakens the relationship between upper 100 m transport and $v'\bar{\theta}$ compared to using the full basin width (Figure 10a). As noted in section 3.2, however, the interannual variability in $v'\bar{\theta}$ obscures the significant linear trend in this term that is relevant for the decadal variability. Partitioning the upper 100 m transport into west and east of 60°E, we find that the trend west of this meridian (−0.14 Sv/decade) is small compared to eastern portion of the basin (0.59 Sv/decade). Thus, even though restricting the upper 100 m transport to the region east of 60°E substantially reduces the ability to account for interannual variations in $v'\bar{\theta}$, it is the eastern portion of the equatorial transect that accounts for the positive linear trend in $v'\bar{\theta}$. Thus, the upper 100 m transport east of 60°E relates to the decadal reversal in in NIO SSH and upper-ocean temperature. The weak trend in the upper 100 m transport west of 60°E suggests that the region dominated by recirculations does not substantially contribute to the decadal variability and is not essential to this analysis. Since the variability east of 60°E is captured by V_{cec} (Figure 10b), we can then reasonably expect a substantial fraction of the decadal trend reversal in $\langle\theta\rangle_{NIO}$ and NIO SSH to be proportional to the time integral of zonal wind stress curl across the basin (see section 4).

We identify particular features of the atmospheric circulation related to variability in V_{cec} by forming composite atmospheric fields during periods of anomalous northward and southward V_{cec} (henceforth V_{cec}^+ and V_{cec}^-, respectively). The periods of V_{cec}^+ and V_{cec}^- are defined as the upper and lower quartiles of V_{cec} calculated from the ERA-Interim wind stress (demarcated by dashed lines in Figure 10). Composite sea level pressure differences (V_{cec}^- minus V_{cec}^+) suggest that forcing of the CEC (i.e., equatorial wind stress curl) is related to the strength and position of the Mascarene High (MH). The MH is a semipermanent anticyclone located to the southeast of Madagascar and is a prominent feature of mean atmospheric circulation over the Indian Ocean (Figure 11a). The strength and position of the MH has basin-wide impacts and has long been known to be closely related to the South Asian Monsoon [e.g., *Krishnamurti and Bhalme*, 1976]. The composite differences show that the MH tends to be displaced northward during periods of V_{cec}^- compared to periods of
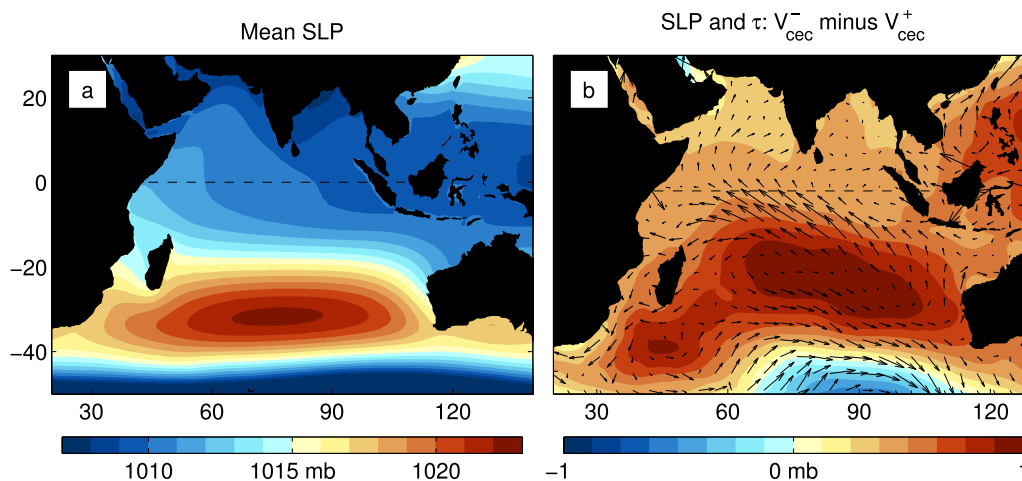
Figure 11. (a) Mean sea level pressure (SLP) over the Indian Ocean from the ERA-Interim reanalysis. Warm colors indicate the mean position of the Mascarene High. (b) Composite differences of SLP (colors) and wind stress vectors (arrows) between periods with anomalous southward cross-equatorial Sverdrup transport (V_{cec}^-) and periods with anomalous northward transport (V_{cec}^+).

V_{cec}^+ (Figure 11b). During these times, anticyclonic winds associated with the MH lead to anomalous easterly wind stress south of the equator, which increases negative equatorial wind stress curl and intensifies southward V_{cec}.

Composite SST differences (V_{cec}^- minus V_{cec}^+) show cool SST anomalies beneath the high SLP anomalies. The SST pattern is reminiscent of the positive phase of the Indian Ocean Subtropical Dipole (IOSD) [*Behera and Yamagata*, 2001] (Figure 12), but with a weaker warm pole southeast of Madagascar. Positive IOSD is characterized by a strengthening and northward expansion of the MH and easterly wind stress anomalies in the tropical South Indian Ocean [*Behera and Yamagata*, 2001]. These results suggest that IOSD events may affect the rate of change in NIO heat content via the coupling of the CEC with the MH.

3.3.2. $w'\bar{\theta}$

Before addressing the forcing of the $w'\bar{\theta}$ term, we highlight an important dynamical link between $v'\bar{\theta}$ and $w'\bar{\theta}$. Since the NIO is bounded in all directions except south, volume conservation requires net vertical volume transport into the upper 700 m of the NIO to be supplied by cold northward cross-equatorial flow below 700 m (beneath our control volume). At the equator, where $f = 0$, Sverdup balance dictates that cross-equatorial flow cannot occur below the mixed layer in the basin interior. As a result, the deep cross-equatorial flow can only occur in the western boundary region. The same net vertical transport must also be compensated by southward cross-equatorial flow across the southern face of the control volume above 700 m. Thus, any mechanism that accounts for variability in $w'\bar{\theta}$ also has an implicit effect on $v'\bar{\theta}$ via this deep overturning cell.

To identify features of the wind stress field related to $w'\bar{\theta}$, we compute composite wind conditions during the upper and lower quartiles of the $w'\bar{\theta}$ time series (Figure 13a). The mean temperature over the bottom face of the NIO volume (i.e., 700 m) is approximately 9.8°C, which is much colder than the mean reference temperature of approximately 14.6°C. Thus, the lower quartile of $w'\bar{\theta}$ corresponds to upwelling velocity anomalies (UPW) with a negative effect on the temperature of the volume. The upper quartile of $w'\bar{\theta}$ corresponds to downwelling velocity anomalies (DNW). Composite differences (UPW minus DNW) of wind stress and wind stress curl (Figure 13b) resemble the pattern obtained by regressing these same fields onto $\langle \tau_x \rangle_A$ in section 2.2 (Figure 5a). Therefore, we use $\langle \tau_x \rangle_A$ as a proxy for the forcing pattern in the composite differences of the wind field. Time series of $\langle \tau_x \rangle_A$ from ECCOv4 and ERA-Interim are significantly anticorrelated to $w'\bar{\theta}$ (Figure 13a; note that the sign of $\langle \tau_x \rangle_A$ is reversed in the figure to aid comparison). The greatest lag correlation between $\langle \tau_x \rangle_A$ and $w'\bar{\theta}$ is $r = -0.73$ for ECCOv4 when the wind stress leads by 3 months, and $r = -0.71$ for ERA-Interim wind stress leading by 2 months.

In section 2.2, we established that even though $\langle \tau_x \rangle_A$ accounts for large fractions of regional SSH variability, $\langle \tau_x \rangle_A$ did not account for variability in basin-mean SSH. In this section, however, we find that the
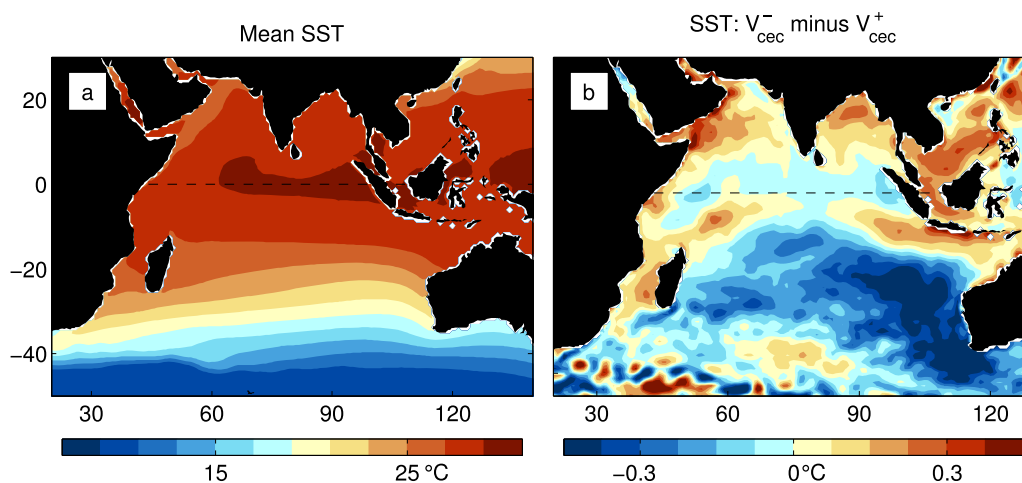
Figure 12. (a) Mean sea surface temperature (SST) over the Indian Ocean from the ERA-Interim reanalysis. (b) Composite differences of SST between periods with anomalous southward cross-equatorial Sverdrup transport (V_{cec}^-) and periods with anomalous northward transport (V_{cec}^+).

wind pattern correlated with $\langle \tau_x \rangle_A$ is related to the *rate of change* in upper-ocean temperature and SSH via the $w'\bar{\theta}$ component of $w\theta$ in (2). We can then expect some fraction of variability in $\langle \theta \rangle_{NIO}$ and NIO SSH to be proportional to $\int_0^t \langle \tau_x \rangle_A \, dt$ (see section 4). As noted above, volume conservation requires net vertical transport across the 700 m face of the control volume to be balanced by export of upper 700 m water across the southern vertical face of the volume. If the transport-weighted mean temperature of the exported water is greater than the reference temperature—i.e., the mean temperature of the control volume—then the effect of $\int_0^t \langle \tau_x \rangle_A \, dt$ on NIO SSH is greater than that suggested by the amplitude of the $w'\bar{\theta}$ term alone. The latter contribution of $\langle \tau_x \rangle_A$ to the tendency of upper-ocean temperature is contained in $v'\bar{\theta}$. The lack of a significant trend in $\langle \tau_x \rangle_A$ indicates that the impact of this forcing on NIO SSH and upper-ocean temperature is not quadratic. Other temporal structures can contribute to the decadal variability, however, by causing deviations from a purely quadratic shape and affecting the timing of zero crossings.

To get a basic understanding of the dynamical relationship between $\langle \tau_x \rangle_A$ and $w'\bar{\theta}$, we regress vertical velocity anomalies at 700 m in ECCOv4, lagged by 3 months, onto $\langle \tau_x \rangle_A$ (Figure 13c). The spatial structure of the regression coefficients is indicative of beta refraction, where Rossby waves propagating from the eastern boundary travel more rapidly closer to the equator. This propagation may account for the lag between $\langle \tau_x \rangle_A$ and $w'\bar{\theta}$. At intraseasonal time scales, low-latitude Rossby waves in the Indian Ocean have deep density and vertical velocity signatures extending to 1000 m and below [*Matthews et al.*, 2010; *Webber et al.*, 2012]. Annual Rossby waves are known to cause even deeper vertical displacements at low southern latitudes in the IO near the southern boundary of the domain considered here [*Johnson*, 2011; *Piecuch and Ponte*, 2014]. Our results suggest that these mechanisms operate on interannual and longer time scales, thereby affecting the rate of change in upper-ocean temperature over the ENIO region. Finally, we note that although the correlation pattern in Figure 13c has a rough north-south symmetry, the deep cross-equatorial flow required by net $w'\bar{\theta}$ must result from north-south asymmetry in basin shape (e.g., the presence of the ITF south of the equator) and/or wind forcing.

3.3.3. $(v'\theta')'$

The $(v'\theta')'$ term results from covariance over a wide range of time scales—primarily those shorter than the interannual scales passed by our low-pass filter. Even the shortest time scales resolved by the monthly mean model output contribute to both the mean and interannual variability of this term. Therefore, we are unable to relate $(v'\theta')'$ in any simple way to low-passed wind forcing indices, such as those identified for the $v'\bar{\theta}$ and $w'\bar{\theta}$ terms.

The long-term mean of the covariance flux ($\overline{v'\theta'}$) is southward and exceeds the amplitude of most interannual and decadal fluctuations in $(v'\theta')'$. The latter does, however, make a nonnegligible contribution to the
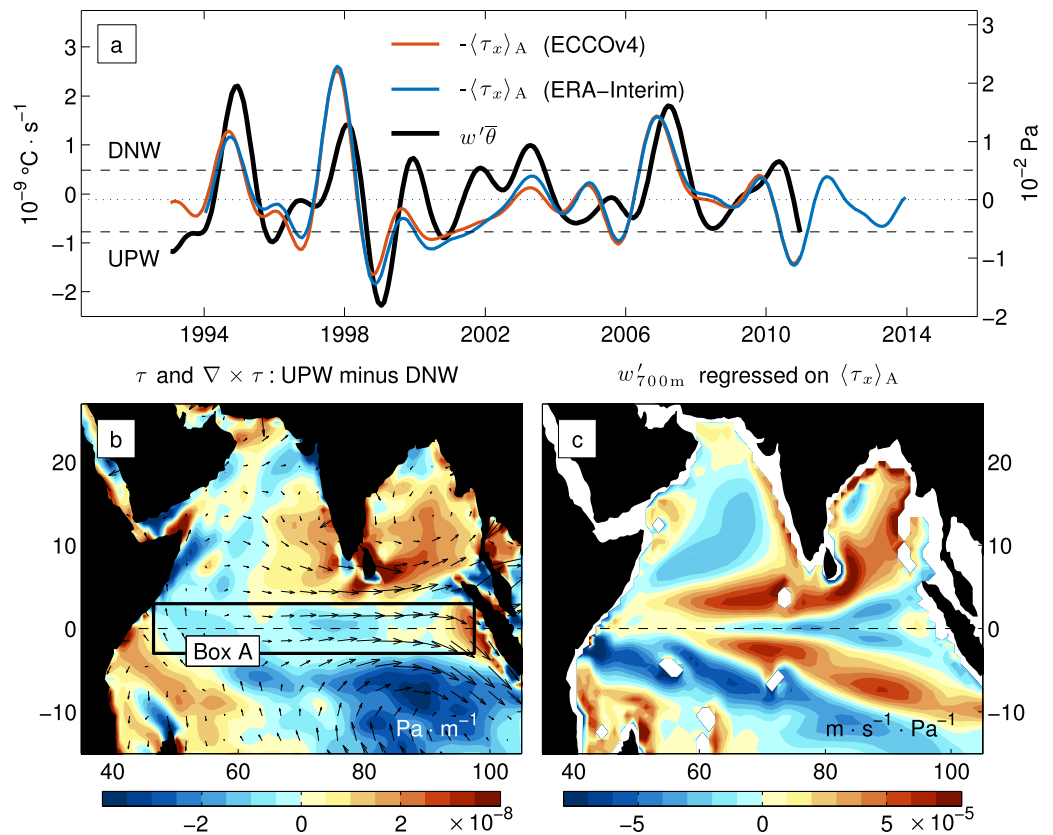
Figure 13. (a) Zonal wind stress averaged over Box A (sign reversed) from ECCOv4 (blue) and ERA-Interim (orange). Potential temperature flux into the upper 700 m of IO north of the equator due to advection of mean potential temperature by vertical velocity anomalies ($w'\bar{\theta}$, black). Dashed lines denote the upper and lower quartiles of $w'\bar{\theta}$ that correspond to anomalous downwelling (DNW) and upwelling (UPW), respectively. (b) Composite differences between UPW and DNW periods for wind stress vectors (arrows) and wind stress-curl (colors). (c) Regression of ECCOv4 vertical velocity anomalies at 700 m (w'_{700m}) onto zonal wind stress averaged in Box A.

decadal variability of $\langle\theta\rangle_{\mathrm{NIO}}$ (Figure 9b). The contribution primarily results from a pulse in the 1997–1998 period (Figure 9a) when the low-passed total covariance flux, $(v'\theta')' + \overline{v'\theta'}$, was briefly positive (not shown). Virtually all of the covariance flux throughout the record is contained in the upper 133 m, which contains 93% of the variance in the full 700 m integral with a correlation coefficient equal to one.

4. Application to Observations

We now return to the SSH observations and test the ability of the wind-forced mechanisms identified in ECCOv4 to account for the spatially coherent decadal SSH variability. Two features of the Indian Ocean wind stress field emerge from the above analyses as leading contributors to the dominant advective terms in the temperature budget. The first is equatorial wind stress curl, which forces the CEC and contributes to upper-ocean temperature and SSH tendency via the $v'\bar{\theta}$ budget term (Figure 10). We use the curl of zonal wind stress averaged in Box A, denoted $\langle\partial_y\tau_x\rangle_A$, as an index for this mechanism. The second important feature is zonal wind stress at the equator, and we use zonal wind stress averaged in Box A, denoted $\langle\tau_x\rangle_A$, as an index for the forcing pattern related to deep vertical transport anomalies (Figure 13). The latter mechanism contributes to both the $w'\bar{\theta}$ and $v'\bar{\theta}$ budget terms.

Both indices relate to upper-ocean temperature *tendency*, and as a result, we use the time integrals of these indices as predictors for basin-scale averages of SSH. We perform simple multiple linear regressions,

$$\langle\eta\rangle = a_1\,p_1 + a_2\,p_2 + \epsilon, \quad \text{where} \tag{5}$$

$$p_1 = \int_0^t \langle\partial_y\tau_x\rangle_A\,dt, \tag{6}$$
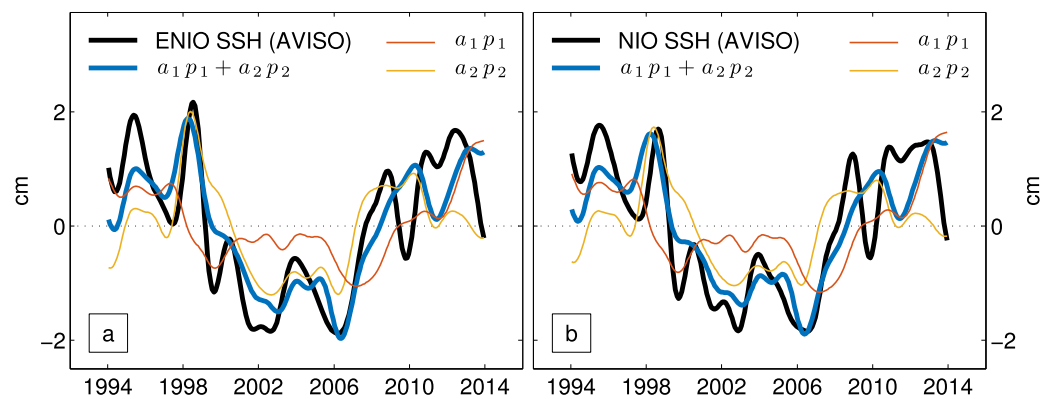
Figure 14. (a) Mean SSH from AVISO north of 5° in the Indian Ocean (ENIO, black); linear least squares best fit to the wind stress predictors defined in the text (blue, see section 4); predictors scaled by their regression coefficients (orange, yellow). The mean is removed from the scaled predictors for direct comparison to the SSH. (b) Same as Figure 14a for the region north of the equator (NIO).

$$p_2 = \int_0^t \langle \tau_x \rangle_A \, dt, \tag{7}$$

$\langle \eta \rangle$ is spatially averaged SSH, a_1, a_2 are the regression coefficients, and ϵ is the residual variability. In practice, we remove the mean and detrend the predictors before performing the regression. We regress AVISO SSH (global mean removed, detrended) averaged over the ENIO (Figure 14a) and NIO (Figure 14b) onto the predictors calculated from ERA-Interim wind stress fields. Together, these two predictors account for more than 70% of the mean SSH variance in both regions, including a majority of the variability at decadal time scales. The fit poorly matches most of the interannual variations.

The two predictors are statistically independent ($r = -0.05$), which means that the variance captured by each individual predictor provides information about the relative importance of the two mechanisms for producing the decadal SSH variability. In the NIO, the two predictors account for approximately the same amount of variance, with p_1 accounting for 38% of the variance in mean SSH and p_2 accounting for 37%. For the ENIO, however, p_1 accounts for just 30% of the variance, while p_2 accounts for 46%. The difference between the geometries of the two regions is, of course, the region between the equator and 5°S. In a regression of mean SSH over this narrow latitude band (not shown), p_1 accounts for only 10% of the variance, while p_2 accounts for 53%. This suggests that the extension of decadal SSH coherence from the NIO across the equator to 5°S (e.g., Figure 2c) primarily results from the north-south symmetry in the forcing pattern related to zonal wind stress at the equator (Figure 13). Based on the regression analysis, the CEC forced by equatorial wind stress curl does not substantially contribute to the SSH variability at the southern extent of the ENIO region.

The independent temporal structure of the two forcing mechanisms produces the phasing of the decadal SSH variability. From time-integrated equatorial wind stress curl (p_1) alone, one would predict an earlier onset of depressed SSH (relative to the global mean) and a later recovery compared to the observations. Time-integrated zonal wind stress (p_2) is less quadratic and more sinusoidal in nature, with end points near zero and a succession of intervals with alternating positive-negative-positive sign. The latter predictor delays the onset of the SSH depression and sustains the negative SSH anomalies during a small recovery toward zero in p_1 during the middle of the altimetry record.

5. Discussion

We do not find a significant contribution of net surface heat flux (Q_{net}) to the ENIO decadal variability in ECCOv4. We note, however, that the time series of Q_{net} anomalies into the ENIO and NIO regions from ECCOv4 differ substantially from the time series of Q_{net} anomalies from the ERA-Interim reanalysis (Figure 15a). More importantly, the temporal integrals of these time series suggest vastly different effects of surface heat flux on upper-ocean temperature and SSH (Figure 15b). Integrated Q_{net} from ECCOv4 corresponds to the surface heat flux contribution to the temperature budget (Figure 7). Based on a simple scaling of the ECCOv4 curves in Figures 7 and 15b, the integrated Q_{net} from ERA-Interim would correspond to mean upper-ocean temperature anomalies in the ENIO region exceeding 0.25°C. Not only is this twice as large as
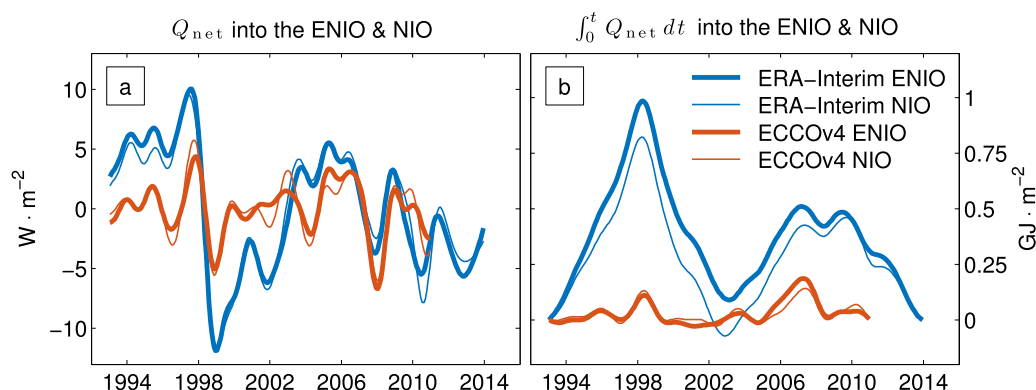
Figure 15. (a) Net surface heat flux (Q_{net}) from ERA-Interim (blue) and ECCOv4 (orange) averaged over the ENIO (thick) and NIO (thin) regions. (b) Same as Figure 15a for the time-integral of Q_{net}. Legend in Figure 15b also applies to Figure 15a.

the greatest anomalies in mean ENIO temperature from ECCOv4, but the temporal structure of the integrated ERA-Interim curve appears quite different than the temporal structure of the observed SSH variability. If the contribution of Q_{net} to the decadal variability is as large as suggested by ERA-Interim, the temporal structure of the integrated Q_{net} is conspicuously absent in the SSH observations.

The differences in Q_{net} between ECCOv4 and ERA-interim most likely result from the ocean fields used to estimate the fluxes. ECCOv4 assimilates near-surface atmospheric fields from ERA-Interim, but fluxes between the ocean and atmosphere are calculated independently using bulk formulae [*Forget et al.*, 2015]. One advantage of ECCOv4 is that the adjoint-based synthesis ensures that the atmosphere, ocean, and flux fields are dynamically consistent. Of course, this does not guarantee that the flux fields are correct, as the result of the synthesis depends on the availability and quality of the assimilated ocean observations. Nevertheless, when combined with the scaling argument above, the dynamical consistency of ECCOv4 fields provides confidence that ECCOv4 Q_{net} represents a more physically reasonable contribution of surface heat flux to ENIO upper-ocean temperature and SSH.

The picture of ENIO decadal variability presented here does not require transfer of heat from the Pacific to the ENIO region as suggested by *Nieves et al.* [2015]. Instead, the ENIO SSH appears to be driven almost entirely by winds over the Indian Ocean that result in low-latitude meridional heat flux variability. It is important to point out, however, that models and observations support increased volume and heat transport during the last 10–15 years into the Indian Ocean via the ITF [e.g., *Lee et al.*, 2015]. The results presented here do not preclude heat transport from the Pacific to the Indian Ocean in recent decades. In fact, ECCOv4 shows an increase in the temperature flux entering the Indian Ocean via the ITF that is similar in timing and magnitude to the recent increase in northward temperature flux into the ENIO. Despite this qualitative similarity, the temperature budget clearly shows that the temperature flux into the ENIO is due to velocity anomalies and is not the result of temperature anomalies advected from the ITF.

While the heat flux into the South Indian Ocean via the ITF does not directly warm the ENIO, warming of the South Indian Ocean could influence the wind-forced mechanisms of intrabasin heat redistribution identified here. Once such pathway is discussed in section 3.3.1, whereby SST anomalies south of the equator imprint on the Mascarene High, which in turn affects forcing of the CEC. In the future, we plan to use ECCOv4 to perform temperature budget and dynamical analyses similar to the present investigation to explore how recent temperature anomalies entering the basin via the ITF circulate in the South Indian Ocean and affect atmospheric circulation over the basin.

6. Summary

A recent reversal in upper-ocean-temperature trends in the ENIO [*Nieves et al.*, 2015] resulted in a spatially coherent increase in the decadal rate of SSH change across the region. A temperature budget for the upper 700 m of the ENIO from ECCOv4 suggests that anomalous circulation acting on the mean temperature field of the ocean (i.e., the $v'\bar{\theta}$ and $w'\bar{\theta}$ budget terms) drives most of the upper-ocean temperature variability.

Thus, redistribution of heat within the Indian Ocean causes the reversal of upper-ocean-temperature trends and the recent increase in the rate of SSH change in the region.

We identify two indices of wind stress variability linked to mechanisms of heat redistribution that capture the decadal variability in a multiple regression. The first is zonal wind stress curl at the equator, which drives the surface branch of the Indian Ocean CEC. The wind stress curl variability relates to the strength and position of the Mascarene High, which is influenced by the phase of the Indian Ocean Subtropical Dipole. The second index is the equatorial, zonal wind stress itself, which is correlated with a wind stress pattern that drives deep (700 m) vertical transport. Because the North Indian Ocean is bounded on three sides, upwelling of cold water at this depth requires northward cross-equatorial flow in the western boundary below 700 m and southward cross-equatorial export of warmer water above 700 m. Together, these two processes caused upper-ocean cooling and suppression of global-mean sea level rise in the ENIO during the first decade of the satellite altimetry record. During the most recent decade, forcing anomalies over the Indian Ocean reversed sign, leading to upper-ocean warming and increasing SSH at a rate exceeding the global-mean rate.

References

Adcroft, A., and J.-M. Campin (2004), Rescaled height coordinates for accurate representation of free-surface flows in ocean circulation models, *Ocean Modell.*, 7(3–4), 269–284, doi:10.1016/j.ocemod.2003.09.003.

Becker, M., B. Meyssignac, C. Letetrel, W. Llovel, A. Cazenave, and T. Delcroix (2012), Sea level variations at tropical Pacific islands since 1950, *Global Planet. Change*, 80–81, 85–98, doi:10.1016/j.gloplacha.2011.09.004.

Behera, S. K., and T. Yamagata (2001), Subtropical SST dipole events in the southern Indian Ocean, *Geophys. Res. Lett.*, 28(2), 327–330, doi:10.1029/2000GL011451.

Cabanes, C., A. Cazenave, and C. Le Provost (2001), Sea level change from Topex-Poseidon altimetry for 1993–1999 and possible warming of the southern oceans, *Geophys. Res. Lett.*, 28(1), 9–12, doi:10.1029/2000GL011962.

Campin, J.-M., J. Marshall, and D. Ferreira (2008), Sea ice ocean coupling using a rescaled vertical coordinate z, *Ocean Modell.*, 24(1–2), 1–14, doi:10.1016/j.ocemod.2008.05.005.

England, M. H., S. McGregor, P. Spence, G. A. Meehl, A. Timmermann, W. Cai, A. S. Gupta, M. J. McPhaden, A. Purich, and A. Santoso (2014), Recent intensification of wind-driven circulation in the Pacific and the ongoing warming hiatus, *Nat. Clim. Change*, 4(3), 222–227, doi:10.1038/nclimate2106.

Forget, G., J.-M. Campin, P. Heimbach, C. N. Hill, R. M. Ponte, and C. Wunsch (2015), ECCO version 4: An integrated framework for non-linear inverse modeling and global ocean state estimation, *Geosci. Model Dev.*, 8(10), 3071–3104, doi:10.5194/gmd-8-3071-2015.

Gadgil, S., P. N. Vinayachandran, P. A. Francis, and S. Gadgil (2004), Extremes of the Indian summer monsoon rainfall, ENSO and equatorial Indian Ocean oscillation, *Geophys. Res. Lett.*, 31, L12213, doi:10.1029/2004GL019733.

Gent, P. R., and J. C. Mcwilliams (1990), Isopycnal mixing in ocean circulation models, *J. Phys. Oceanogr.*, 20(1), 150–155, doi:10.1175/1520-0485(1990)020 < 0150:IMIOCM>2.0.CO;2.

Heimbach, P., C. Hill, and R. Giering (2005), An efficient exact adjoint of the parallel MIT General Circulation Model, generated via automatic differentiation, *Future Gener. Comput. Syst.*, 21(8), 1356–1371, doi:10.1016/j.future.2004.11.010.

Johnson, G. (2011), Deep signatures of southern tropical Indian Ocean Annual Rossby waves, *J. Phys. Oceanogr.*, 41, 1958–1964, doi:10.1175/JPO-D-11-029.1.

Kosaka, Y., and S.-P. Xie (2013), Recent global-warming hiatus tied to equatorial Pacific surface cooling, *Nature*, 501(7467), 403–407, doi:10.1038/nature12534.

Krishnamurti, T. N., and H. N. Bhalme (1976), Oscillations of a monsoon system. Part I. Observational aspects, *J. Atmos. Sci.*, 33(10), 1937–1954, doi:10.1175/1520-0469(1976)033 < 1937:OOAMSP>2.0.CO;2.

Lee, S.-K., W. Park, M. O. Baringer, A. L. Gordon, B. Huber, and Y. Liu (2015), Pacific origin of the abrupt increase in Indian Ocean heat content during the warming hiatus, *Nat. Geosci.*, 8(6), 445–449, doi:10.1038/ngeo2438.

Lee, T., I. Fukumori, and B. Tang (2004), Temperature advection: Internal versus external processes, *J. Phys. Oceanogr.*, 34(8), 1936–1944, doi:10.1175/1520-0485(2004)034 < 1936:TAIVEP>2.0.CO;2.

Marshall, J., A. Adcroft, C. Hill, L. Perelman, and C. Heisey (1997a), A finite-volume, incompressible Navier Stokes model for studies of the ocean on parallel computers, *J. Geophys. Res.*, 102(C3), 5753–5766, doi:10.1029/96JC02775.

Marshall, J., C. Hill, L. Perelman, and A. Adcroft (1997b), Hydrostatic, quasi-hydrostatic, and nonhydrostatic ocean modeling, *J. Geophys. Res.*, 102(C3), 5733–5752, doi:10.1029/96JC02776.

Matthews, A. J., P. Singhruck, and K. J. Heywood (2010), Ocean temperature and salinity components of the Madden-Julian oscillation observed by Argo floats, *Clim. Dyn.*, 35(7–8), 1149–1168, doi:10.1007/s00382-009-0631-7.

Merrifield, M. A. (2011), A shift in Western Tropical Pacific Sea Level Trends during the 1990s, *J. Clim.*, 24(15), 4126–4138, doi:10.1175/2011JCLI3932.1.

Miyama, T., J. P. McCreary, T. G. Jensen, J. Loschnigg, S. Godfrey, and A. Ishida (2003), Structure and dynamics of the Indian-Ocean cross-equatorial cell, *Deep Sea Res., Part II*, 50(12–13), 2023–2047, doi:10.1016/S0967-0645(03)00044-4.

Nidheesh, A. G., M. Lengaigne, J. Vialard, A. S. Unnikrishnan, and H. Dayan (2012), Decadal and long-term sea level variability in the tropical Indo-Pacific Ocean, *Clim. Dyn.*, 41(2), 381–402, doi:10.1007/s00382-012-1463-4.

Nieves, V., J. K. Willis, and W. C. Patzert (2015), Recent hiatus caused by decadal shift in Indo-Pacific heating, *Science*, 349(6247), 532–535, doi:10.1126/science.aaa4521.

Oliver, E. C. J., and K. R. Thompson (2010), Madden-Julian Oscillation and sea level: Local and remote forcing, *J. Geophys. Res.*, 115, C01003, doi:10.1029/2009JC005337.

Piecuch, C. G., and R. M. Ponte (2014), Annual cycle in Southern Tropical Indian Ocean bottom pressure, *J. Phys. Oceanogr.*, 44(6), 1605–1613, doi:10.1175/JPO-D-13-0277.1.

Saji, N. H., B. N. Goswami, P. N. Vinayachandran, and T. Yamagata (1999), A dipole mode in the tropical Indian Ocean, *Nature*, 401(6751), 360–363, doi:10.1038/43854.

Schwarzkopf, F. U., and C. W. Böning (2011), Contribution of Pacific wind stress to multi-decadal variations in upper-ocean heat content and sea level in the tropical south Indian Ocean, *Geophys. Res. Lett.*, *38*, L12602, doi:10.1029/2011GL047651.

Shankar, D., S. G. Aparna, J. P. McCreary, I. Suresh, S. Neetu, F. Durand, S. S. C. Shenoi, and M. A. Al Saafani (2010), Minima of interannual sea-level variability in the Indian Ocean, *Prog. Oceanogr.*, *84*(3–4), 225–241, doi:10.1016/j.pocean.2009.10.002.

Timmermann, A., S. McGregor, and F.-F. Jin (2010), Wind Effects on Past and Future Regional Sea Level Trends in the Southern Indo-Pacific, *J. Clim.*, *23*(16), 4429–4437, doi:10.1175/2010JCLI3519.1.

Trenary, L. L., and W. Han (2013), Local and remote forcing of decadal sea level and thermocline depth variability in the South Indian Ocean, *J. Geophys. Res. Oceans*, *118*, 381–398, doi:10.1029/2012JC008317.

Webber, B. G. M., A. J. Matthews, and K. J. Heywood (2010), A dynamical ocean feedback mechanism for the Madden-Julian Oscillation, *Q. J. R. Meteorol. Soc.*, *136*, 740–754, doi:10.1002/qj.604.

Webber, B. G. M., A. J. Matthews, K. J. Heywood, and D. P. Stevens (2012), Ocean Rossby waves as a triggering mechanism for primary Madden-Julian events, *Q. J. R. Meteorol. Soc.*, *138*(663), 514–527, doi:10.1002/qj.936.

Webster, P. J., A. M. Moore, J. P. Loschnigg, and R. R. Leben (1999), Coupled ocean atmosphere dynamics in the Indian Ocean during 199798, *Nature*, *401*(6751), 356–360, doi:10.1038/43848.

Willis, J. K., D. Roemmich, and B. D. Cornuelle (2004), Interannual variability in upper ocean heat content, temperature, and thermosteric expansion on global scales, *J. Geophys. Res.*, *109*, C12036, doi:10.1029/2003JC002260.

Wunsch, C., and P. Heimbach (2013), Dynamically and kinematically consistent global ocean circulation and ice state estimates, in *Ocean Circulation and Climate: A 21st Century Perspective, vol. 103 of International Geophysics*, edited by G. Siedler et al., chap. 21, pp. 553–579, Academic, Oxford, U. K., doi:10.1016/B978-0-12-391851-2.00021-0.